




Genetic algorithm-based inverse design of elastic gridshells

Longhui Qin¹ · Weicheng Huang¹ · Yayun Du¹ · Luocheng Zheng¹ · Mohammad Khalid Jawed¹ 

Received: 15 January 2020 / Revised: 24 April 2020 / Accepted: 25 May 2020
© Springer-Verlag GmbH Germany, part of Springer Nature 2020, corrected publication 2020

Abstract

An initially two-dimensional grid of elastic rods may be actuated into a three-dimensional shell-like structure, through buckling, when the end-points of the rods are constrained to a shrunk boundary. The shape of the 3D gridshell is a joint result of elasticity and geometric constraint. We develop a discrete differential geometry-based model of elastic gridshell to investigate their form-finding process. Even though the forward process from 2D footprint to 3D gridshell can be captured by physics-based simulation, the inverse problem of obtaining the original footprint given the 3D deformed shape still lacks a generalized method. In this paper, we propose a genetic algorithm (GA)-based inverse design method to explore the planar footprint of an elastic gridshell as well as the corresponding geometric constraints. Geometric features extracted from the original planar form are encoded into various chromosomes to constitute a population in every generation. With the fitness function constructed based on the deviation of the candidate solution from the 3D target shape, the population evolves gradually until the individual of the smallest fitness value representing the optimal footprint and final boundary constraints is found under seven predefined geometric constraints. Given a series of representative target shapes, e.g., hemispherical cap, paraboloid structure, Gaussian curve shape, and semi-ellipsoid, their original footprints are quantified using a network of 10 elastic rods. Excellent agreement is obtained between the prescribed 3D shape and the simulated buckled structures as small fitness value is obtained and little difference between them is observed, which validates the effectiveness of the proposed GA-based inverse design method.

Keywords Elastic gridshell · Buckling instability · Form finding · Numerical simulation · Genetic algorithm

1 Introduction

Elastic gridshell refers to a network of elastic rods linked by joints (Pai 2002; Spillmann and Teschner 2009). Planar gridshells would buckle and deform into a three-dimensional (3D) shell-like structure when their extremities are loaded, which is a synthetic result of geometric constraints and elasticity. Spanning from microscopic to macroscopic scale, a variety of researches have been conducted

focusing on elastic gridshells involved in abundant applications, such as assembly of micro nanomaterial (Xu et al. 2015), performance optimization of gridshell structures (Richardson et al. 2013; Jiang et al. 2018), and construction of gridshell buildings (Quagliaroli and Malerba 2013; Tayeb et al. 2013; Lefevre et al. 2015).

The compressive buckling process suggests that a functional mapping relationship exists between the planar footprint and the actuated 3D structure. To simulate this process, plenty of methods have been developed falling into 3 categories: stiffness matrix method, geometric stiffness method, and dynamic equilibrium method (Veenendaal and Block 2012). Given an initial geometric boundary and certain stress state, these methods tend to update the system configuration in small steps, which iterates until a steady state of force equilibrium is obtained. Based on these methods, a number of prior works addressed the problem of form finding with different optimization objectives. A numerical form-finding method was proposed to find the minimal surface of membrane structures, in which a gradient method in the Hilbert space was

Responsible Editor: Mehmet Polat Saka

Longhui Qin and Weicheng Huang contributed equally to this work.

✉ Mohammad Khalid Jawed
khalidjm@seas.ucla.edu

¹ Department of Mechanical and Aerospace Engineering, University of California, Los Angeles, Los Angeles, CA 90095, USA

applied (Shimoda and Yamane 2015). Su et al. (2019) established structural analysis model and conducted finite element analysis in order to solve the problem of form-finding problem of reciprocal structure, a special structural system, whose shape was then optimized by minimizing the total strain energy under static loads. With the objective of material minimization and improved structural performance, dynamic relaxation method with kinetic damping was used to determine the global grid shell form and up to 50% of material mass was reduced (Richardson et al. 2013). Achieving the maximum stiffness or improving the load carrying behavior was used as an optimization goal in similar form-finding problems (Shimoda et al. 2018; Firl and Bletzinger 2012). In the field of discrete differential geometry (DDG) (Grinspun et al. 2006), numerical tools for geometry processing and physical simulation have been used in numerous applications related to form-finding, e.g., finding the appropriate architectural and structural shape (Coenders and Bosia 2006). Promising in animating knots, sutures, plants, and kinematic skeletons, the mechanical model of elastic rods is ideal for modeling deformations induced by stretching, bending, or twisting (Bergou et al. 2008; Bergou et al. 2010; Jawed et al. 2018). Rod-based models are, therefore, a natural choice to simulate gridshells. Discrete elastic rods (DER), based on Kirchhoff's rod theory (Kirchhoff 1859), is a DDG-based computationally efficient simulation tool, which has been validated against experiments. Excellent agreement was found between numerical simulation and physical experiment when DER was applied to model the coiling of elastic rod onto a moving substrate (Jawed et al. 2014), flexible helical rod rotating in a viscous fluid (Jawed et al. 2015), and the buckling process of elastic gridshell (Baek et al. 2018).

The forward process for an elastic gridshell to be actuated from a planar footprint to a 3D structure can be simulated with the aforementioned simulation tools including DER. However, most researches on form-finding problems are aimed at seeking an optimal shape in a state of static equilibrium (Veenendaal and Block 2012). Only a small portion of the prior works in this field focused on the inverse process, i.e., how to determine the original footprint when the 3D structure is given as a target. A functional mapping relationship, $G_O(x, y) \in \mathbb{R}^2 \rightarrow G_F(x, y, z) \in \mathbb{R}^3$, exists due to the interaction of elasticity and geometric constraints. This is difficult to be modeled using classical methods because of the geometrically nonlinear deformation of the elastic rods constituting the gridshell. For example, the household strainer is a gridshell of hemispherical shape, whose planar form before deformation resembles a rounded diamond instead of a circle. Baek et al. (2018) utilized the continuum theory

of smooth Chebyshev net (Chebyshev 1946) to find the original form, G_O , and the theoretical result was compared against DER simulations and experimental prototypes. Considering the complexity from buckled structures to original footprints and shrunk constraint boundaries, an evolutionary computational method, genetic algorithm (GA), is introduced, which is able to find a global solution in a space consisting of candidate solutions inspired by natural genetic variation and natural selection (Mitchell 1998). Therein a fitness function of low-cost evaluation is critical and will facilitate GA to be efficient in processing multiple-variable optimization problems. Compared with purely local methods (e.g., gradient descent), genetic algorithms have the advantage that they do not necessarily remain trapped in a suboptimal local maximum or minimum of the target function (Rojas 2013). Moreover, GA has shown good performance in similar fields, such as truss topological optimization (Hajela and Lee 1995), form finding of tensegrity structures (Koohestani 2012), inverse design of ribbon-shaped structures (Xu et al. 2019), and generation of initial pre-stress forces to maximize elastic buckling load (Dini et al. 2013). It is also capable of facilitating multi-objective optimization of free-form grid structures (Winslow et al. 2010) and determination of bar orientation for gridshells to minimize the stresses (Bouhaya et al. 2014). As the fitness of every individual is required to be calculated in real-time during the evolution process, it, thus, raises the need for a computationally efficient mechanics-based simulation that maps 2D footprints to 3D buckled structures.

In this paper, to explore the original footprint of the actuated shell-like structures, we develop an improved discrete gridshell simulation and propose a GA-based inverse design method under a set of geometric constraints. A fully implicit algorithm is developed to characterize the mechanical behavior of the gridshell comprised of multiple elastic rods. Compared with the semi-explicit algorithm used in previous works (Baek et al. 2018), the improved discrete gridshell model is more robust, shows better convergence behavior, and allows us to take larger time steps. Combination of the improved gridshell model and GA is used to solve the inverse problem associated with form-finding. Moreover, an area-approximation-based method is used to produce an efficient initial chromosome. A series of examples are presented. Hemispherical, paraboloid, and Gaussian surfaces are used as target 3D structures that are symmetric about $x = y$ and $x = -y$ axis. Semi-ellipsoid is taken as a case where the boundary constraints are asymmetric about $x = y$ and $x = -y$ axis. Geometric parameters of the planar footprint as well as the final positions of the end-points of the rods, based on a network of 10 elastic rods (5 along the x -axis and 5 along the y -axis), are unknown and encoded into a chromosome. Based

on the fitness values of the solution obtained from GA, apparent comparison in 3D surface, and 2D outline of cross-sections, good agreements are found between the theoretical surfaces and the 3D structures actuated from the optimal 2D footprints under certain boundary constraints, which are solved by the proposed method. In addition, examples are presented where the number of elastic rods in the gridshell is increased to 26. Results show that the proposed inverse design method is still applicable to the gridshells constructed with more elastic rods.

2 Problem description

Figure 1 shows a planar gridshell consisting of 10 elastic rods located on the $x - y$ plane. Among them, 5 rods are parallel to the x -axis while the other 5 are parallel to the y -axis. Therein, the length and position of every elastic rod is unknown, i.e., positions of every rod end (x_i, y_i) are to be determined. To simplify the problem, the definition of an elastic gridshell in this paper is assumed to follow two conditions: (1) Every rod is symmetric about both the x - and y -axis. (2) Spacing between every two adjacent elastic rods (either in x or y direction) is equal to d_x or d_y . With this definition, a footprint will be regarded as the same when it rotates about the vertical z -axis. In Fig. 1b, when the extremities of all the elastic rods (i.e., the first and last nodes on each rod) are moved to the circular points, the footprint will buckle and deform into a 3D shell-like structure. In this example, the outermost form of both the footprint in Fig. 1a and the final constraint boundary in Fig. 1b are set to be circular as an example. Therein the curve connecting the ends of all elastic rods as shown in Fig. 1b is the shrunk constraint boundary. The mapping relationship can be represented by $G_O(x, y) \in \mathbb{R}^2 \rightarrow G_F(x, y, z) \in \mathbb{R}^3$.

Considering that the footprint and the final shape of interest are symmetric about the x - and the y -axes, a quarter of the structure is taken to study the geometries of the original footprints and the final boundaries. Instead of Cartesian coordinates (x_i, y_i) , polar coordinates (R_{xi}, θ_{xi}) and (R_{yi}, θ_{yi}) are used, as it makes geometric constraints easier to be defined and visualized. The original and final geometries are shown in Fig. 1c and d, respectively. Since the final constraint boundary is known in advance from the given target shape, only the polar angles $(\theta_{xi}, \theta_{yi})$ of the rod's ends are the unknowns. The final constraint boundary connected all the end-points of the rods is a circular shape in cases I–III: hemisphere, paraboloid, and Gaussian surface. In case IV, i.e., semi-ellipsoid, the boundary is an ellipse. The variable θ_{Fxi} (and θ_{Fyi}) denotes the orientation angle of the i th rod end on the final constraint boundary if the rod was parallel to the x -axis (and the y -axis) in undeformed

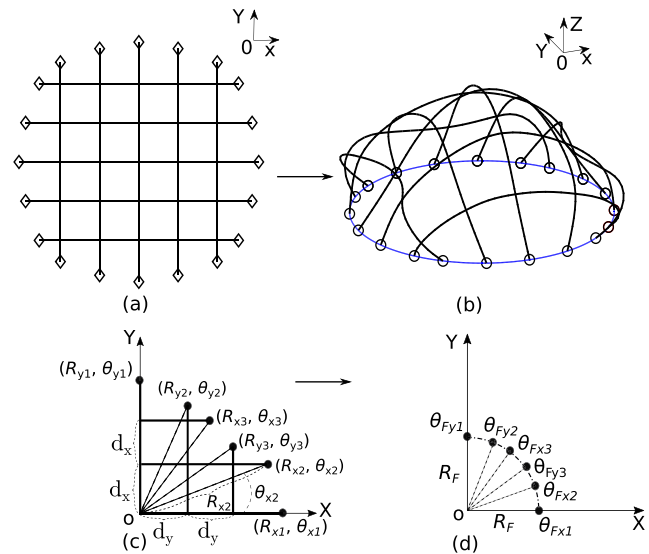


Fig. 1 Geometries of original footprint and its boundary constraint. **a** Elastic gridshell consisting of 10 crossed elastic rods. **b** 3D structure buckled via DER with blue circle denoting the final boundary constraint. **c** A quarter of geometry of the elastic gridshell, which can be determined by parameter pairs (R_{xi}, θ_{xi}) and (R_{yi}, θ_{yi}) . d_x and d_y are the distance between adjacent rods along x - and y -axis. **d** A quarter of geometry of final boundary constraint, in which only angles of every rods end need to be determined for given boundary form

2D shape. For the first three cases, hemisphere (case I), paraboloid (case II), and Gaussian surface (case III), the final constraint boundary is a circle. In the last case of a semi-ellipsoid (case IV), the boundary outline is an ellipse. Analytical expressions defining these four surfaces are

$$\Gamma(x, y, z) : x^2 + y^2 + z^2 - r_F^2 = 0, \quad (1)$$

$$\Gamma(x, y, z) : \frac{x^2}{r_F^2} + \frac{y^2}{r_F^2} + \frac{z}{h_P} - 1 = 0, \quad (2)$$

$$\Gamma(x, y, z) : A_G \cdot e^{-\frac{x^2+y^2}{2\sigma^2}} - A_G \cdot e^{-\frac{r_F^2}{2\sigma^2}} - z = 0, \text{ and } (3)$$

$$\Gamma(x, y, z) : \frac{x^2}{a_E^2} + \frac{y^2}{b_E^2} + \frac{z^2}{c_E^2} - 1 = 0, \quad (4)$$

where r_F is the radius of the final circular boundary (in this paper $r_F = 0.5$); h_P characterizes the height of the paraboloid (set to be 0.25); $A_G = 0.5$ and $\sigma = 0.3$ are respectively the height of the Gaussian curve's peak and the standard deviation controlling its width; $a_E = 0.5$ and $b_E = 0.3$ are respectively the length of the semi-major axis and semi-minor axis of the final constraint boundary of the ellipse; and c_E defines its height ($c_E = 0.2$ in this paper).

Two geometric constraints (GCs) can be constructed from the above discussion for an elastic gridshell consisting

of total $N_x + N_y$ rods, where N_x rods are initially oriented along the x -axis and N_y rods positioned along the y -axis.

$$\theta_{x1} = 0 \text{ and } \theta_{y1} = \pi/2, \quad (\text{GC1a})$$

$$\theta_{Fx1} = 0 \text{ and } \theta_{Fy1} = \pi/2, \quad (\text{GC1b})$$

$$(j-1) R_{xi} \sin \theta_{xi} = (i-1) R_{xj} \sin \theta_{xj}, \quad i, j = 2, \dots, (N_x + 1)/2, \quad (\text{GC2a})$$

$$(m-1) R_{yk} \cos \theta_{yk} = (k-1) R_{ym} \cos \theta_{ym}, \quad k, m = 2, \dots, (N_y + 1)/2. \quad (\text{GC2b})$$

Equation (GC1aa) is applies to the original footprint while (GC1ab) stands for the final constraint boundary. Combined, they indicate that both the boundaries before and after deformation are symmetric about the x - and y -axis. Equation (GC2a) is a statement of equidistance between two adjacent rods along the x - and the y -axis in the initial 2D shape. In addition, the original and final boundaries are symmetric about $x = y$ and $x = -y$ axes for cases I to III. With (GC2a), the input dimension can be further reduced. After all, the geometric parameters to be determined are $(R_{x1}, R_{x2}, \theta_{x2}, \theta_{x3}, \theta_{Fx2}, \theta_{Fx3})$ for cases I to III when $N_x = N_y = 5$. However, 12 parameters $(R_{x1}, R_{x2}, R_{y1}, R_{y2}, \theta_{x2}, \theta_{x3}, \theta_{y2}, \theta_{y3}, \theta_{Fx2}, \theta_{Fx3}, \theta_{Fy2}, \theta_{Fy3})$ need to be determined for semi-ellipsoid since it is asymmetric about $x = y$ and $x = -y$ axis. It should be noted, due to multiple possible modes of buckling, the same footprint can lead to two different 3D shapes. However, in practice, such possibility is rare and is not addressed in this paper.

3 Mechanical model of the discrete gridshell

Different from traditional 2D plates and shells, gridshell consists of a network of 1D elastic rods, and, therefore, classical plate and shell theories cannot be directly applied to explore the mechanical properties of this special structure. In prior numerical investigations (Baek et al. 2018), the DER algorithm (Bergou et al. 2008; Bergou et al. 2010) was extended to discrete gridshell model, where the cross points between two elastic rods are modeled by a stiff spring and the spring force was applied explicitly (Euler forward). In this section, we comparatively describe two methods of simulating such structures—(1) a spring-based method and (2) a *mapping* method that does not require any springs. In case of the spring-based method, the spring force is handled in two different ways—(1) explicitly and (2) implicitly.

3.1 DER algorithm

As a key component of gridshell structure, the forward physics-based simulation of a single elastic rod will

be described first. DER algorithm was first introduced in the computer graphics community for simulating the dynamic behavior of hair and other filamentary structures in the animation industry, which then solved plenty of engineering problems successfully. In Kirchhoff's theory of elastic rods (Kirchhoff 1859), the rod centerline is represented by an arc-length parameterized curve, $\gamma(s)$, and the angular evolution of the tangent aligned orthonormal material director is described by $\theta(s)$. The deformation of Kirchhoff's rod can be characterized with three quantities: bending curvature $\kappa(s)$, twist $\tau(s)$, and axial stretch $\epsilon(s)$. Referring to Fig. 2, we discretize the continuous rod centerline into N nodes, $[\mathbf{x}_0, \mathbf{x}_1, \dots, \mathbf{x}_{N-1}]$, and $N-1$ edges, $[\mathbf{e}^0, \mathbf{e}^1, \dots, \mathbf{e}^{N-2}]$, with $\mathbf{e}^i = \mathbf{x}_{i+1} - \mathbf{x}_i$. We follow the convention of using subscripts for node-based quantities and superscripts for edge-related parameters. Associated with each of $N-1$ edges are the reference frame $\{\mathbf{d}_1^i, \mathbf{d}_2^i, \mathbf{t}^i\}$, the orthonormal material frame $\{\mathbf{m}_1^i, \mathbf{m}_2^i, \mathbf{t}^i\}$, and the turning angle between these two frames θ^i . The discretized elastic rod can be regarded as a system containing $4N-1$ degrees of freedom (DOF), $\mathbf{q} = [\mathbf{x}_0, \theta^0, \mathbf{x}_1, \theta^1, \dots, \mathbf{x}_{N-2}, \theta^{N-2}, \mathbf{x}_{N-1}]$ (Bergou et al. 2008; Bergou et al. 2010). These DOFs are updated with time based on the equations of motion, as described next.

Stretching Uniaxial deformation along each edge can be easily formulated by its original length $|\bar{\mathbf{e}}^i|$ and deformed length $|\mathbf{e}^i|$ through

$$\epsilon^i = \frac{|\mathbf{e}^i - \bar{\mathbf{e}}^i|}{|\bar{\mathbf{e}}^i|}. \quad (5)$$

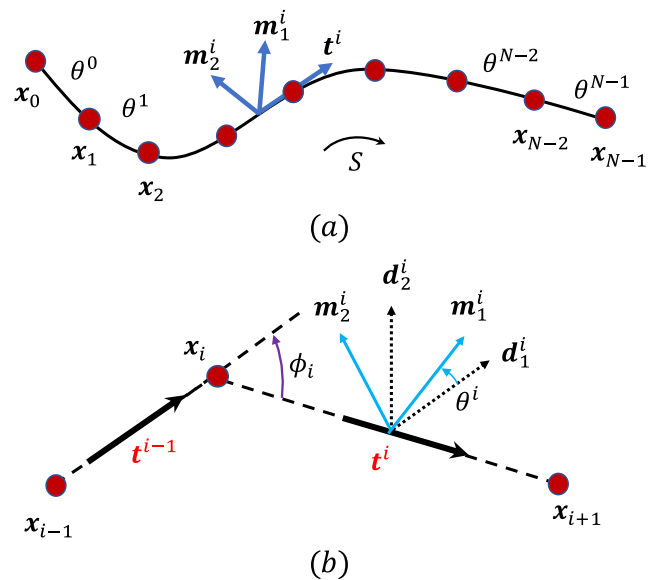


Fig. 2 **a** Geometric discretization of 1D elastic rod model; **b** Schematic of the relevant quantities of elastic rod deformation

The elastic energy related to uniaxial strain can be written as

$$E_s = \sum_{i=0}^{N-2} \frac{1}{2} EA (\epsilon^i)^2 |\bar{\mathbf{e}}^i|, \quad (6)$$

where EA is the stretching stiffness of elastic rod.

Bending The material curvatures associated with node \mathbf{x}_i are

$$\kappa_i^{(1)} = \frac{1}{2} (\mathbf{m}_2^{i-1} + \mathbf{m}_1^i) \cdot (\kappa \mathbf{b})_i, \quad (7a)$$

$$\kappa_i^{(2)} = -\frac{1}{2} (\mathbf{m}_1^{i-1} + \mathbf{m}_1^i) \cdot (\kappa \mathbf{b})_i, \quad (7b)$$

where \mathbf{m}_1^i , \mathbf{m}_2^i , \mathbf{m}_1^{i-1} and \mathbf{m}_2^{i-1} are directors of the material frame, and $(\kappa \mathbf{b})_i$ is the curvature binormal,

$$(\kappa \mathbf{b})_i = \frac{2\mathbf{e}^{i-1} \times \mathbf{e}^i}{|\mathbf{e}^{i-1}| |\mathbf{e}^i| + \mathbf{e}^{i-1} \cdot \mathbf{e}^i}. \quad (8)$$

Note that the magnitude of $(\kappa \mathbf{b})_i$ is related to the turning angle ϕ_i ,

$$|(\kappa \mathbf{b})_i| = 2 \tan \frac{\phi_i}{2}. \quad (9)$$

The bending energy of elastic rod can be written as

$$E_b = \sum_{i=0}^{N-1} \frac{1}{2} \frac{EI}{l_i} \left[(\kappa_i^{(1)} - \bar{\kappa}_i^{(1)})^2 + (\kappa_i^{(2)} - \bar{\kappa}_i^{(2)})^2 \right], \quad (10)$$

where $\bar{\kappa}_i^{(1)}$ and $\bar{\kappa}_i^{(2)}$ are the undeformed curvatures at the i -th node, and $l_i = \frac{1}{2} (|\mathbf{e}^i| + |\mathbf{e}^{i+1}|)$ is the vertex-based Voronoi length, and EI is the bending stiffness. Here, it is assumed that material properties of our rod model is isotropic.

Twisting The twisting curvature associated with each node \mathbf{x}_i is

$$\tau_i = \theta^i - \theta^{i-1} + \underline{m}_i, \quad (11)$$

where \underline{m}_i is the reference twist of the reference frame. Details behind its computation can be found in Jawed et al. (2018). The twisting energy, similar to previous stretching and bending energy, can be written as a quadratic term,

$$E_t = \sum_{i=0}^{N-1} \frac{1}{2} \frac{GJ}{l_i} (\tau_i - \bar{\tau}_i)^2, \quad (12)$$

where $\bar{\tau}_i$ is undeformed twist and GJ is the twisting stiffness of elastic rod.

The total elastic energy of the rod is

$$E^{\text{int}} = E_s + E_b + E_t. \quad (13)$$

Equation of motion At each time step, with the DOF vector \mathbf{q} and its velocity $\dot{\mathbf{q}}$ known, we need to solve the equation of

motion to obtain the DOF vector and its velocity at the next time step,

$$f_j \equiv m_j \frac{q_j(t + \Delta t) - q_j(t)}{\Delta t^2} - m_j \frac{\dot{q}_j(t)}{\Delta t} - f_j^{\text{int}} - f_j^{\text{ext}} = 0, \quad (14)$$

where q_j is the j -th element of \mathbf{q} , $0 \leq j \leq 4N - 2$, m_j is the mass associated with each DOF, the elastic internal force f_j^{int} on the j -th DOF can be evaluated by the gradient of elastic energy, $f_j^{\text{int}} = -\frac{\partial E^{\text{int}}}{\partial q_j}$, and f_j^{ext} is the external force, e.g., gravity. The linear system of equations can be solved fully implicitly by Newton-Raphson method,

$$\mathbf{q}^{n+1}(t + \Delta t) = \mathbf{q}^n(t + \Delta t) - \mathbf{J}^n / \mathbf{f}^n, \quad (15)$$

where the superscript n denotes the number of iteration, the elements of the vector \mathbf{f} can be evaluated using (14), and \mathbf{J}^n is the Jacobian matrix whose elements are

$$J_{jk} = \frac{m_j}{\Delta t^2} \delta_{jk} + \frac{\partial^2}{\partial q_j \partial q_k} E^{\text{int}} - \frac{\partial}{\partial q_k} f_j^{\text{ext}}, \quad (16)$$

where δ_{jk} is the Kronecker delta. Note that the Jacobian matrix of rod-like structure is a banded matrix, as shown in Fig. 3. The computational complexity of this simulation is, therefore, $O(N)$.

3.2 Interaction between two elastic rods

The DER model is insufficient to simulate elastic gridshells, without considering the joint between two elastic rods at the intersection point. As shown in Fig. 4a, the simplest method to model the intersection point is a stiff spring, i.e., a penalty energy. Here, we only consider the translational constraints between two rods at the joint point and ignore the rotational constraints, i.e., the coupled rods can rotate freely at the joint. The non-trivial bending and twisting

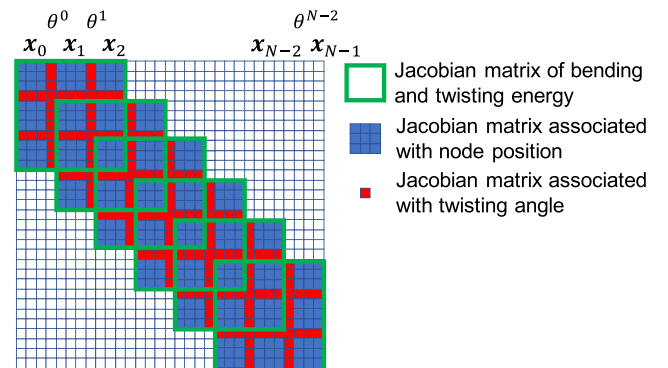
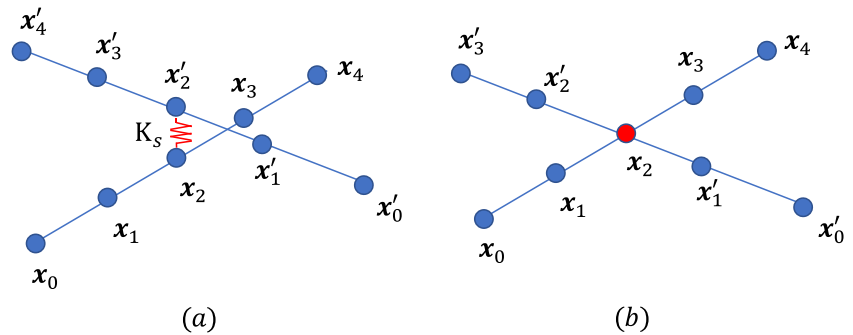


Fig. 3 Jacobian matrix of elastic rod structure. As the bending and twisting energy at node \mathbf{x}_i is only related to \mathbf{x}_{i-1} , \mathbf{x}_{i+1} , θ^{i-1} , and θ^i , the Jacobian matrix is a banded matrix

Fig. 4 **a** Modeling of elastic gridshells with two separate rods connected by a stiffed spring. **b** Modeling of elastic gridshells with mapping method



coupling between two rods at joints can be found in Pérez et al. (2015) and Panetta et al. (2019). Previous numerical investigation of elastic gridshells adopted the spring-based method (Baek et al. 2018), in which a gridshell is modeled by multiple independent rods coupled with springs and the spring force is treated in an explicit approach. However, the value of the spring stiffness in this method is crucial: it can be neither too large nor too small. In the former case, there will be a deviation between two rods at the intersection point, while the simulator may not converge in the latter case at any reasonable size of time step.

Implicit spring method We build a new DOF vector $\tilde{\mathbf{q}}$ that contains DOF vectors of all $m \equiv (N_x + N_y)$ rods in gridshells,

$$\tilde{\mathbf{q}} = [\mathbf{q}_0, \mathbf{q}_1, \dots, \mathbf{q}_r, \dots, \mathbf{q}_m], \quad (17)$$

where \mathbf{q}_r is the DOF vector of the r -th rod with size $(4N - 1)$ and N is the total number of nodes of the r -th rod. Referring to Fig. 4a, if a node \mathbf{x}_2 on one rod is very close to another node \mathbf{x}'_2 on another rod, a linear spring between the two is introduced. The energy of the spring, $E^{\text{cons}} = \frac{1}{2} k_s \frac{|\mathbf{x}_2 - \mathbf{x}'_2|^2}{|\bar{\mathbf{x}}_2 - \bar{\mathbf{x}}'_2|}$, is added to the expression for elastic energies in (13), where $|\bar{\mathbf{x}}_2 - \bar{\mathbf{x}}'_2|$ is the distance between \mathbf{x}_2 and \mathbf{x}'_2 in the undeformed configuration. If the initial

distance is zero, we use a small length of $1 \times 10^{-6} \text{m}$ in the denominator to avoid numerical singularity. The gradient and Hessian corresponding to the spring energy can be trivially computed. All the free DOFs of all the rods in (17) are solved together using Newton-Raphson and the spring forces, similar to the elastic forces, are treated implicitly. Figure 5b shows the non-zero elements of the Jacobian matrix for the simple structure in Fig. 4a. As shown in Fig. 5b, the Jacobian matrix is no longer banded; the interaction between \mathbf{x}_2 and \mathbf{x}'_2 contributes to the non-zero entries, $\frac{\partial^2 E^{\text{cons}}}{\partial \mathbf{x}_2 \partial \mathbf{x}'_2}$, outside the diagonal band.

Mapping method If the spring stiffness is not large enough, implicit method may suffer from inaccuracies where the two nodes at the intersection points are not perfectly coincident. Rather than treating the two nodes from two different rods at the crossing point separately, a single node is used in the mapping method to represent the crossing point. The discretization of the rods is slightly changed so that \mathbf{x}_2 and \mathbf{x}'_2 coincide in the undeformed configuration. As shown in Fig. 4b, \mathbf{x}_2 is assumed to be part of both the elastic rods and the elastic force on this node is the sum of elastic forces computed from two separate rods. With this method, the spring is not necessary any more and the problem of choosing an appropriate spring stiffness is naturally resolved. The number of DOF of the whole

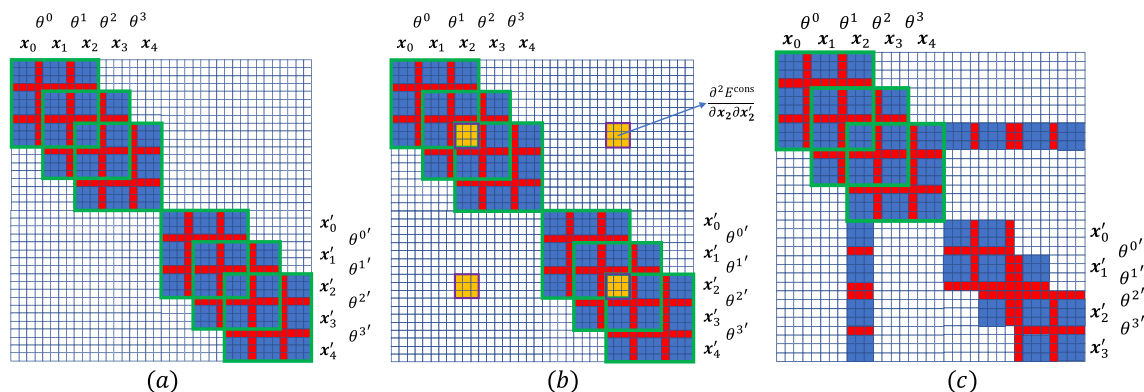


Fig. 5 Non-zero entries of the Jacobian matrix in three different methods for the simplest element of a gridshell structure. **a** Jacobian matrix of explicit method. **b** Jacobian matrix of implicit method. **c** Jacobian matrix of mapping method

system is reduced by $T \times 3$, where T is the number of crossing points. Figure 5c shows the Jacobian matrix in this method.

3.3 Simulation loop

In case of the explicit spring method, the system of equations in (14) is independently solved for each rod, with the spring forces at the joints treated as the external forces, to update the DOFs. At the end of the time step, the spring forces are calculated using these DOFs and applied in the subsequent time step. The Jacobian matrix corresponding to the spring forces is zero, i.e., the term $\frac{\partial}{\partial q_k} f_j^{\text{ext}}$ in (16) is ignored. In the simulation, we applied a Dirichlet boundary condition such that the positions of the first and the last nodes on each rod are constrained to move from the original footprint to the final boundary. The velocity associated with these boundary conditions are slow enough that the process can be treated as quasi-static and the role of inertia is negligible. All other DOFs are *free* and evolves based on the equations of motion.

For the implicit spring method, all the DOFs of all the rods in (17) are updated by solving the equations of motion. The configuration of one rod may be coupled with another one due to the spring forces at the joints. Unlike the explicit spring method, the Jacobian matrix for the spring forces are not ignored. In case of the mapping method, no spring force is used and the DOFs of the gridshell evolve based on the balance of elastic forces. The boundary conditions remain the same as in the explicit spring method.

4 GA-based inverse design method

In order to find out the initial footprint mentioned in Section 2, GA is combined with the discrete gridshell simulation described in the last section. Figure 6 shows a flowchart of the GA-based inverse design method. After population initialization, geometric parameters and the final constraint boundary are assigned by a set of guessed values, which are entered into the discrete gridshell model. Then the 3D buckled structure is simulated and the fitness function is calculated from the simulation. In the diamond-shaped block in Fig. 6, whether the stopping criteria have been met is judged. These criteria include the maximum generation number threshold, fitness function value, variation of the best fitness, etc. The population will evolve via three GA operators—selection, crossover, and mutation—until the stopping criteria are met. Thus the whole process will iterate until one of the stopping criteria is reached, when optimal geometries of the original footprint and final constraint boundary are outputted.

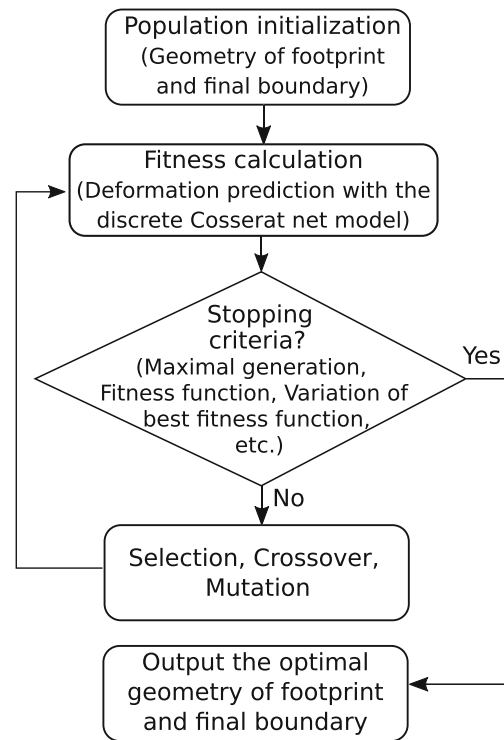


Fig. 6 Flowchart of the GA-based inverse design method

4.1 Geometric constraints

In addition to (GC1a) and (GC2a), five additional geometric constraints as shown in Fig. 7 are defined next in (GC3a) to (GC7) for a realizable solution. The first constraint as shown in Fig. 7a is

$$L_{xb} \leq R_{xi} \leq U_{xb}, \quad (\text{GC3a})$$

$$L_{yb} \leq R_{yj} \leq U_{yb}, \quad (\text{GC3b})$$

$$L_{\theta_x} \leq \theta_{xi}, \theta_{Fxi} \leq U_{\theta_x}, \quad (\text{GC3c})$$

$$L_{\theta_y} \leq \theta_{yj}, \theta_{Fyj} \leq U_{\theta_y}, \quad (\text{GC3d})$$

where L_{xb} and U_{xb} are the lower and upper bounds on the rod length along the x -axis while L_{yb} and U_{yb} are those along the y -axis; L_{θ_x} , U_{θ_x} , L_{θ_y} and U_{θ_y} are the lower and upper bounds on the angles. Based on (GC3a), R_{xi} , R_{yi} ($i = 1, 2$), and θ_{xj} , θ_{Fxi} , θ_{yk} , θ_{Fyj} ($j = 2, 3, \dots, N_x$, $k = 2, 3, \dots, N_y$), are generated first. Then the other radii are calculated according to (GC2a) to meet the equidistance requirement. Especially, θ_{x1} , θ_{y1} , θ_{Fxi} , and θ_{Fyj} are zeros in order to maintain these two rods on x and y -axis before and after actuation. The radii calculated from (GC2a) should be checked to ensure that they satisfy (GC3a).

The next constraint in (GC4a) is used to ensure that at least one joint exists between every elastic rod and the gridshell. Otherwise, one or more elastic rods may be

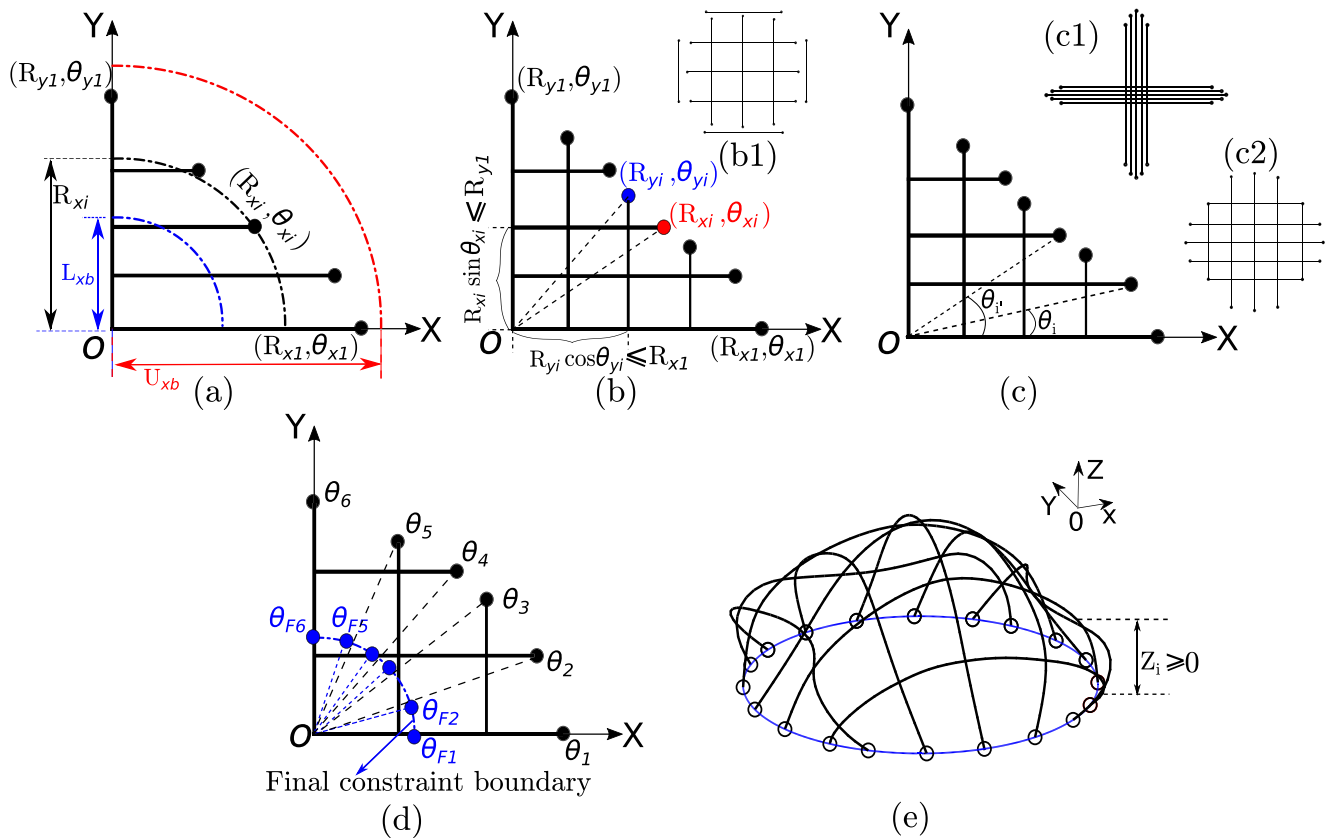


Fig. 7 Five geometric constraints (a) ~ (e) corresponding to (GC3a)~(GC7) respectively. (b1) is a possible gridshell if (GC4a) is not met. (c1) and (c2) are two possible gridshells if (GC5a) is not met

independent from the whole network, such as the gridshell given in Fig. 7b1.

$$R_{xi} \cdot \sin \theta_{xi} \leq R_{y1}, \quad (\text{GC4a})$$

$$R_{yi} \cdot \cos \theta_{yj} \leq R_{x1}. \quad (\text{GC4b})$$

In order to favor an even distribution of rods, an optional constraint is

$$|\theta_i - \theta_{i'}| \geq L_\theta, \quad (\text{GC5a})$$

$$|\theta_{Fi} - \theta_{Fi'}| \geq L_{F\theta}, \quad (\text{GC5b})$$

where L_θ and $L_{F\theta}$ are threshold values set by the user to protect any two rods from getting too close to each other in the original footprint and final constraint boundary, respectively; $|\cdot|$ denotes the absolute value operator; θ_i and $\theta_{i'}$ represent two distinct angles from the set of angles θ_{xi} with $i = 1, \dots, (N_x + 1)/2$ (or θ_{yj} with $j = 1, \dots, (N_y + 1)/2$); and θ_{Fi} and $\theta_{Fi'}$ are two distinct angles from θ_{Fxi} (or θ_{Fyj}). Possible footprints if (GC5a) is not satisfied are shown in Fig. 7c1, where the distance between two adjacent elastic rods is too small, and Fig. 7c2, where the end-points of two rods are located too close to one another.

Moreover, it should be avoided that an elastic rod overlaps with another one at a point near the ends. This condition can be enforced with (GC6):

$$\theta_{Fi} \leq \theta_{Fj} \quad (\text{GC6})$$

if $\theta_i \leq \theta_j$, where $1 \leq i, j \leq (N_x + N_y)/2 + 1$. The geometric representation can be found in Fig. 7d.

The last constraint is the exclusion of solutions involving 3D gridshells with part of the structure under ground. Assuming that the outward normal to the ground is the positive z -axis, any node $\mathbf{x}_i \equiv (x_i, y_i, z_i)$ on the gridshell after deformation should satisfy (GC7) as shown in Fig. 7e.

$$z_i \geq 0 \quad (\text{GC7})$$

It is worth noting that (GC3a) to (GC6) should be checked before the candidate solutions are inputted into the simulation, which will help exclude invalid solutions in advance to reduce the computational cost. Equation (GC7) can only be checked after the 3D buckled structure is outputted from the simulation.

Based on these geometric constraints, the problem of interest in this paper can be expressed as:

$$\begin{aligned} &\text{Given } \Gamma(x, y, z) \in \mathbb{R}^3, \\ &\text{find } G_O(x, y) \in \mathbb{R}^2, \text{ and } \mathbb{C}_F(x, y), \\ &\text{that minimizes } |\Gamma(x, y, z) - \hat{\Gamma}(x, y, z)|, \\ &\text{subject to} \\ &\hat{\Gamma}(x, y, z) = f(G_O(x, y) | \mathbb{C}_F(x, y)), \text{ and } GC1 \sim GC7 \end{aligned} \quad (18)$$

where $\mathbb{C}_F(x, y)$ is the final shrunk constraint boundary consisting of all rod ends and $f(G_O(x, y) | \mathbb{C}_F(x, y))$ denotes the buckling process, via which the original footprint $G_O(x, y)$ will be actuated to the 3D surface $\hat{\Gamma}(x, y, z)$ under $\mathbb{C}_F(x, y)$.

4.2 GA configuration

To start with GA, the variables to be determined are first encoded into an individual, i.e., chromosome. As described in Section 2, six variables need to be evaluated for cases I to III. They can be encoded as $\{R_{x1}, R_{x2}, \theta_{x2}, \theta_{x3}, \theta_{Fx2}, \theta_{Fx3}\}$. Twelve variables for case IV will be encoded as $\{R_{x1}, R_{x2}, R_{y1}, R_{y2}, \theta_{x2}, \theta_{x3}, \theta_{y2}, \theta_{y3}, \theta_{Fx2}, \theta_{Fx3}, \theta_{Fy2}, \theta_{Fy3}\}$.

500 such individuals consist a population, which evolves for at least 50 generations and at most 150 generations. The related GA parameters are provided in Table 1. Therein, R_{LB} (and θ_{LB}) and R_{UB} (and θ_{LB}) denote the lower bound and upper bound on radius (and polar angle), respectively. Maximum and minimum numbers of generation are G_{max} and G_{min} , respectively. Number of individuals contained in a population is N_P . The fractions r_{se} , r_{cr} and r_{mu} represent the rate of selection, crossover, and mutation, respectively; note that $r_{se} + r_{cr} + r_{mu} = 1$. $r_{se} = 0.05$ is the portion of individuals among the parent population that will be selected and passed on to the child population according to the stochastic universal sampling (SUS) method (Baker 1987). $r_{cr} = 0.65$ indicates that most children are produced via combining the chromosomes of their parents. Child is formed in a way that it is more similar to the parent of better fitness. It can be formulated as child = “ratio · (parent1 – parent2) + parent2, where ratio is set to be 1.4. The remaining $r_{mu} = 0.3$ portion of individuals produce their children in an adaptive feasible way of mutation.

Table 1 Parameter configuration of GA

R_{LB}	R_{UB}	θ_{LB}	θ_{LB}	G_{max}
1.0	3.0	0	$\pi/2$	150
G_{min}	N_P	r_{se}	r_{cr}	r_{mu}
50	500	0.05	0.65	0.3

4.3 Population initialization

The evolution process will be time-consuming and unpredictable if every produced individual must meet all the geometric constraints. In order to save time, fitness computation of the individuals unsatisfying the geometric constraints will be skipped and assigned a fitness value of infinity. However, in this way, the GA process may quickly run out of the threshold value of 150 generations without an optimal solution. To avoid this situation, a valid and relatively feasible solution, as outlined next, should be provided to initialize the chromosome at the beginning.

After deformation, the 3D buckled structure has a surface area approximately equal to the original footprint. For cases I to III, a 2D circular shape of the same surface area as the deformed structure is regarded as a guess of the initial solution. The radius of the guessed initial circle is

$$R_I = \sqrt{\frac{\iint_S \sqrt{f_x^2 + f_y^2 + 1} dA}{\pi}}, \quad (19)$$

where $z = f(x, y)$ is the formula of the 3D surface in (1) to (4), and f_x and f_y are the partial derivatives of $f(x, y)$ with respect to x and y , respectively. For case IV, an ellipse with the same surface area as the target 3D shape is taken as the initial guess shown. The semi-major axis, R_{Ia} , and semi-minor axis, R_{Ib} , of this guessed ellipse are

$$R_{Ia} = \sqrt{\frac{\iint_S \sqrt{f_x^2 + f_y^2 + 1} dA \cdot a_E}{\pi b_E}}, \quad (20a)$$

$$R_{Ib} = \sqrt{\frac{\iint_S \sqrt{f_x^2 + f_y^2 + 1} dA \cdot b_E}{\pi a_E}}. \quad (20b)$$

Although it is difficult to give a formulation for a general structure, two criteria could provide a direction to construct such an initial chromosome: (1) The initial footprint shares an approximately equal surface area with the buckled 3D surface. (2) A shape of the initial footprint that is similar to the final constraint boundary may be a possible initial guess.

4.4 Fitness function

Fitness function in GA guides the whole evolution process. Figure 8 shows the flowchart of this function. The aforementioned geometric constraints as well as whether the simulation will converge in certain solutions will be checked in the fitness function. Those violating the required conditions will be assigned a fitness value of infinity. GA will always facilitate the whole population evolve along the direction in which a smaller fitness value is achieved.

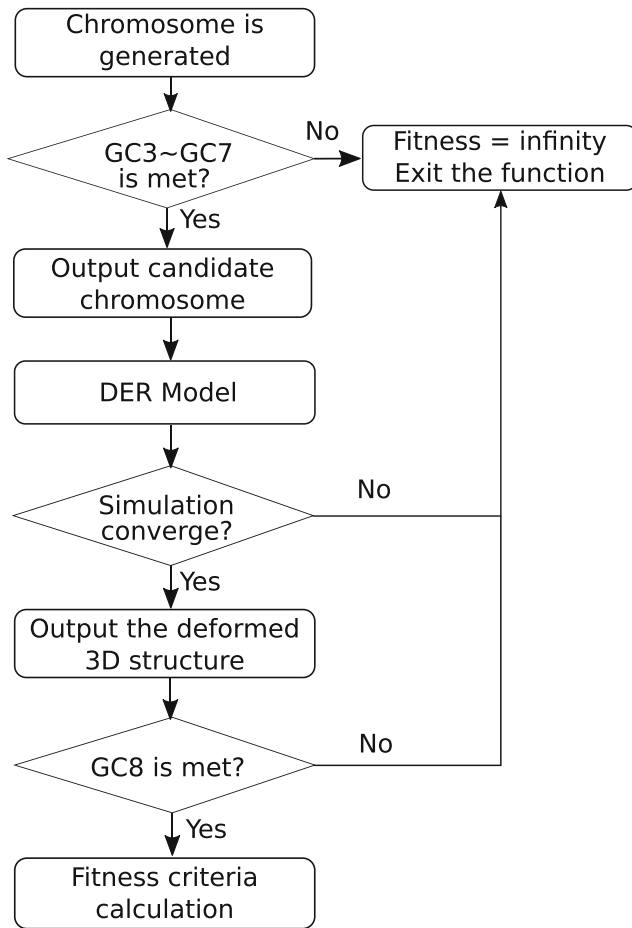


Fig. 8 Flowchart of the fitness function

The nodal positions from the 3D buckled surface, which are outputted from the discrete gridshell simulation, are inputted into the formula of the target surface $\Gamma(x, y, z)$ to be built. The notion of equivalent radius is introduced next in (21) to help evaluate the fitness.

$$R_{Eq} = \left(\frac{3}{2} \pi \cdot V \right)^{1/3} \quad (21)$$

where V is the volume underneath the 3D buckled surface defined in (1) to (4). Physically, R_{Eq} is the radius of a hemisphere whose volume is equal to the 3D structure surrounded by the elastic gridshell to be built. Based on it, the fitness criterion can be calculated using the following expression,

$$\text{fitness} = \frac{1}{N_p \cdot R_{Eq}} \sum_{i=1}^{N_p} |\Gamma(x', y', z')| \quad (22)$$

where N_p is the total number of nodes ($P(x', y', z')$) in the elastic gridshell. A smaller fitness value indicates a better match between the buckled structure and the target surface.

It should be noted that the fitness value is the average difference of all nodes in the target shape and the actuated 3D surface, normalized by the equivalent radius R_{Eq} . It is different than the error between the equivalent radius of the target shape and that of the actuated 3D surface.

5 Results and discussions

In this section, geometries of original footprints and final constraint boundary found by the proposed method will be presented. Via a comparison with theoretical surfaces, the fitness of solution will be also analyzed and discussed.

5.1 Performance of the discrete gridshell model

To compare performance of the three methods mentioned in Section 3, they are applied to model the process of shrinking

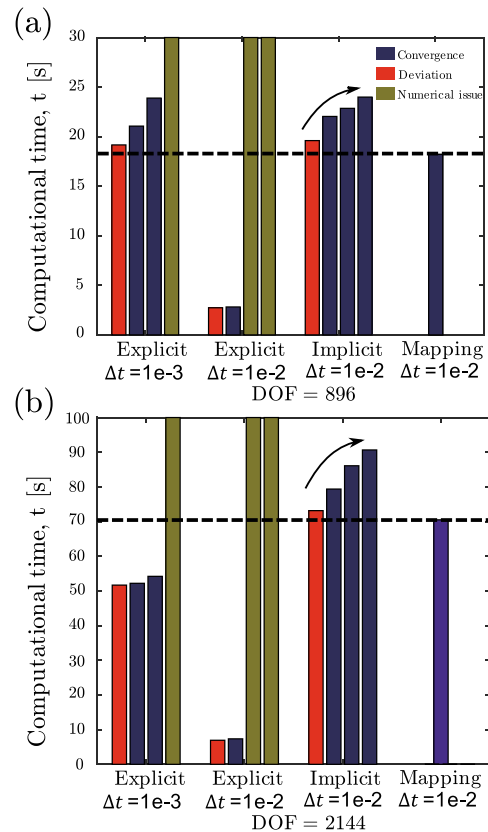


Fig. 9 Comparison among explicit method, implicit method, and mapping method. **a** DOF = 896 (for mapping method, DOF = 800); **b** DOF = 2144 (for mapping method, DOF = 2048). The four bars in each of the first three clusters represent the computation time at four different values of spring stiffness—0.1EI, 1EI, 10EI and 100EI—from left to right. The computation time when there is numerical issue is ∞

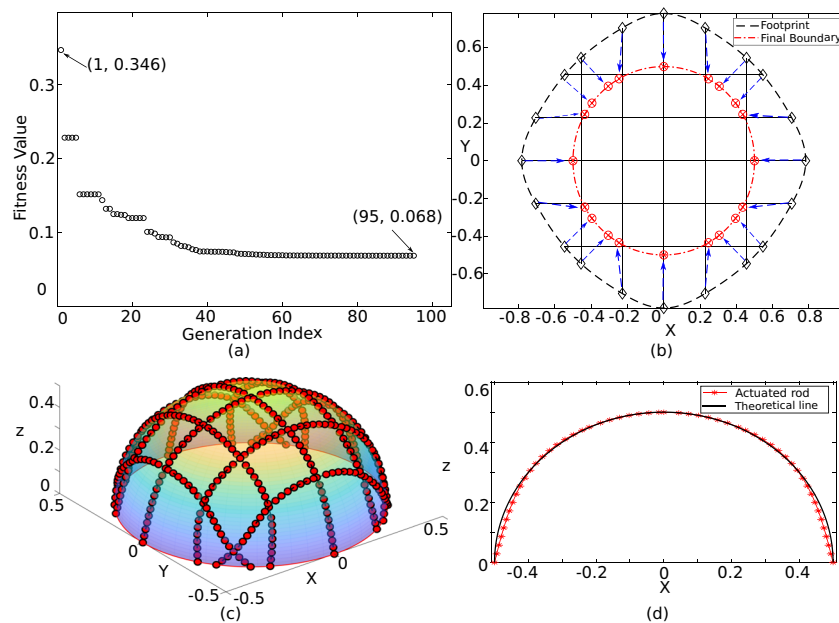


Fig. 10 Design of hemispherical gridshell based on GA. **a** Variation of fitness value with generation index. The marked points indicate the initial fitness value and the total generation number of evolution process as well as the final fitness. **b** Original footprint and the final constraint boundary. Dashed line indicates the original footprint before deformation. Vertical and horizontal solid lines represent elastic rods with the diamond symbols denoting the two ends of each rod.

an initially planar circular gridshell with radius $\rho_0 = 0.5$ m to a 3D buckled structure constrained by a circle of radius $\rho = 0.4$ m. The physical parameters used in the simulation are: Young's modulus $E = 1$ GPa, Poisson's ratio $\nu = 0.5$ (incompressible material), rod radius $r_0 = 1$ cm, number of rods $m = 10$ (5 rods along the x -axis and 5 along the y -axis), boundary velocity $v = 0.01$ m/s, and total time $T = 12$ s, which is larger than $(\rho_0 - \rho)/v$. The boundary velocity is slow enough and the total time is long enough

The arrows indicate the imposed displacement on the extremities of the rods to transform the initially planar shape to the target shape. **c** Deformed 3D structure and the target hemisphere (semi transparent surface). Solid circles represent the nodes after deformation in the discrete gridshell model. Therein the red points are the discrete nodes in simulation. **d** Comparison of the buckled elastic rod in the plane $y = 0$ and the target circular shape

that the overall process is quasi-static. Figure 9 shows a comparison of the computation time and convergence performance among the three methods. The only difference between Fig. 9a and b is the number of degrees of freedom. As indicated in the caption, Fig. 9a uses a more coarsely discretized elastic gridshell and, therefore, requires smaller computation time.

In this bar chart, the first cluster of four bars represents the computation time using the explicit spring method at

Fig. 11 Buckling process to get a hemisphere using the discrete gridshell model. Snapshots at **(a)** $t = 0$ s, **b** $t = 1$ s, **c** $t = 2$ s, and **d** $t = 10$ s. The final constraint boundary is shown by the circle at $z = 0$

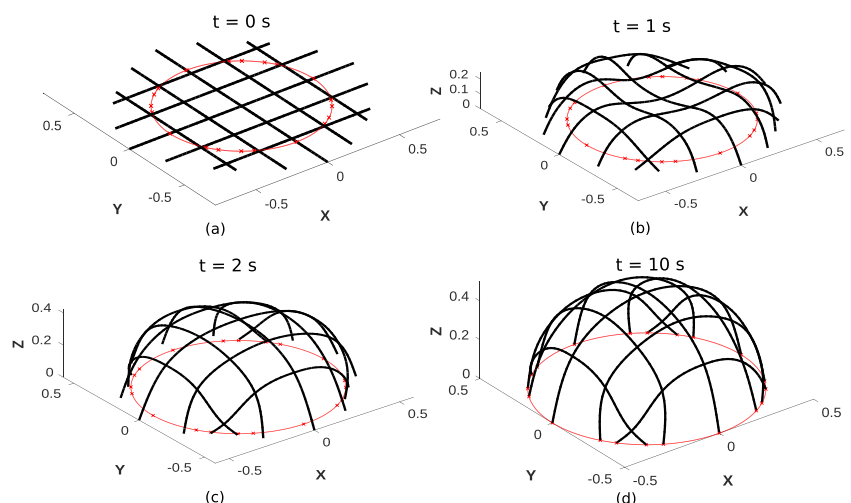
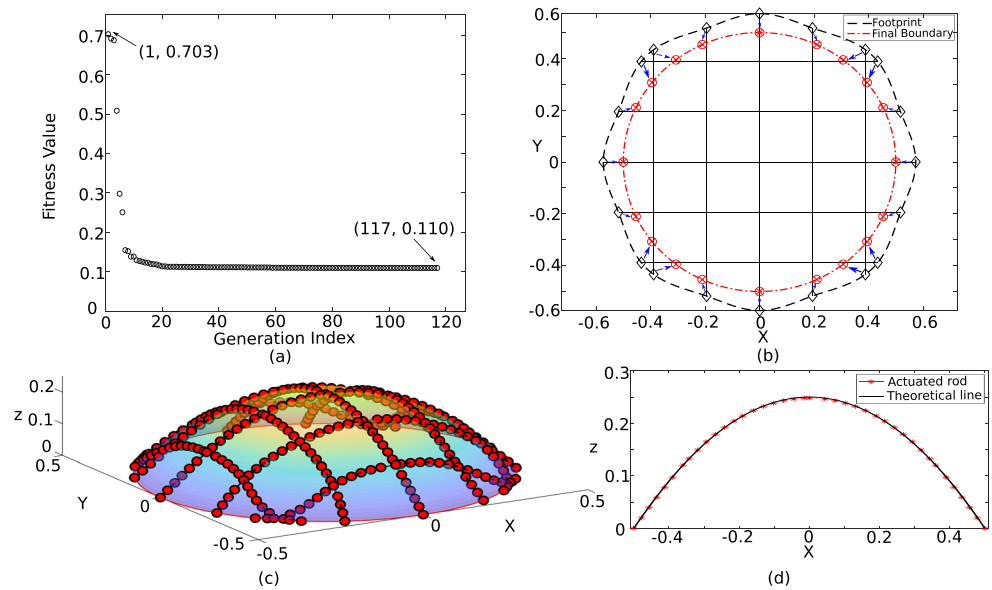


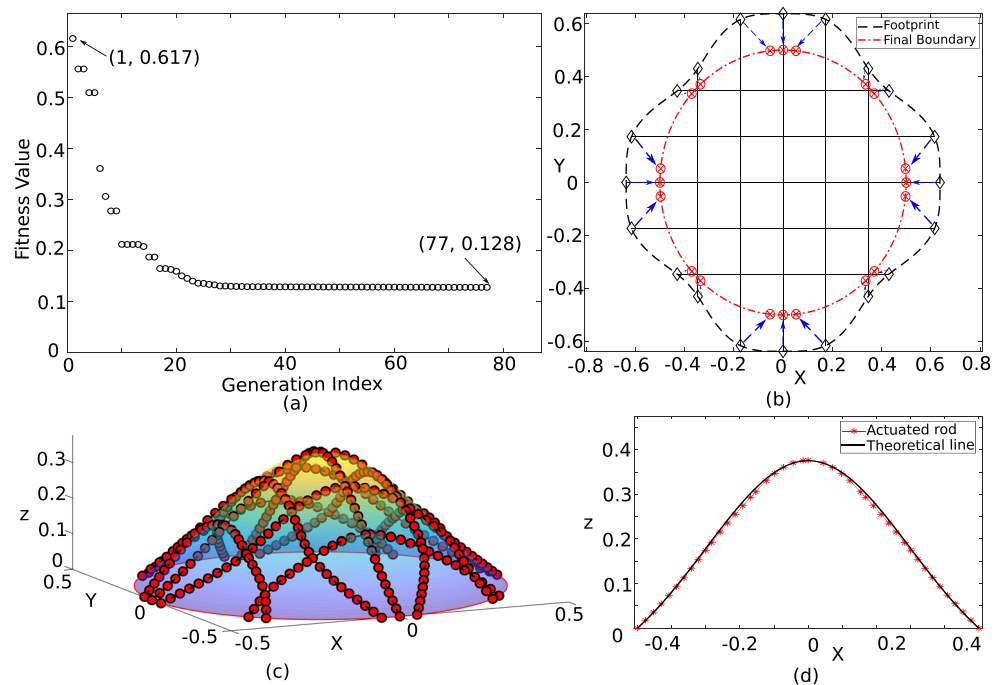
Fig. 12 Design of paraboloid gridshell based on GA. **a** Variation of fitness value with respect of generation index. **b** Original footprint and final constraint points. **c** Deformed 3D structure and the target paraboloid. **d** Comparison of buckled elastic rod in the plane $y = 0$ and the target parabola



four different stiffness numbers— $k_s \in \{0.1EI, 1EI, 10EI, 100EI\}$ —at a time step size of $\Delta t = 10^{-3}$ s. The simulation converges to the correct solution only when k_s is $1EI$ or $10EI$. If the spring stiffness is lower, the simulation reaches a solution that is incorrect due to the excessive softness of the spring. If the spring stiffness is greater, the simulation fails to converge at this time step. The next cluster of four bars shows the computation time with a larger time step size of $\Delta t = 10^{-2}$ s. In this case, the simulation only converges to the correct solution if $k_s = 1EI$. However, the

computation time is noticeably smaller, compared with the previous case of $\Delta t = 10^{-3}$. In contrast with the explicit spring method that mostly fails to converge at $\Delta t = 10^{-2}$, the implicit spring method—represented by the third cluster of bars in Fig. 9—can reach the correct solution at all values of spring stiffness except at $k_s = 0.1EI$. There is no noticeable difference in computation time between the explicit and implicit spring method. In short, implicit spring method typically allows larger time step size and does not strongly depend on the value of the spring stiffness.

Fig. 13 Design of Gaussian gridshell based on GA. **a** Variation of fitness value with respect of generation index. **b** Original footprint and final constraint points. **c** Deformed 3D structure and the target Gaussian surface. **d** Comparison of buckled elastic rod in the plane $y = 0$ and the target Gaussian curve



The last bar in Fig. 9 shows the computation time for the mapping method. The simulation converges at $\Delta t = 10^{-2}$ s and, as discussed earlier, the springs at the joints are no longer necessary. We no longer run into the problem of picking the value of the spring stiffness that can influence the simulation results. The computation time is slightly lower than the one with implicit spring method.

5.2 Symmetric cases (cases I to III)

In cases I to III, the footprints, final boundaries, and deformed 3D structures after buckling are symmetric about the x -axis, the y -axis, $x = y$, and $x = -y$. After simplification, only 6 parameters need to be evaluated to determine the original footprint as well as the final constraint boundary.

Result of case I—hemisphere—is shown in Fig. 10. As shown in Fig. 10a, the initial fitness value in the first generation is 0.346 and the initial guess is described in (19). The evolution process stopped after running 95 generations since the fitness value had remained unchanged for many generations and the final fitness value is 0.068. The variation curve indicates that our initial guess provides a valid candidate chromosome in finding the original form and final constraint position, based on which the population evolves fast from the first to the 23rd generation. It is a rough searching period, which is followed by a finer searching period. In Fig. 10b, the vertical and horizontal elastic rods constitute an elastic gridshell, within which the

distance between two adjacent vertical or horizontal rods is $d_x = d_y = 0.2279$ m. A piecewise cubic interpolation method was used to fit the extremities of the elastic rods to construct the outermost boundary. The original footprint resembles a rounded rectangular shape and is almost identical to the analytical solution using the theory of smooth Chebyshev nets (Baek et al. 2018). Then, the rod's extremities (first and last nodes) displaced along the arrows to finally reach the circular final constraint boundary.

The buckled 3D structure is shown in Fig. 10c. Circle symbols are the discrete nodes in the simulation. In comparison with the theoretical hemisphere, excellent agreement is obtained between the target and the simulated 3D structure. For an even closer comparison, Fig. 10 d shows the elastic rod located in the plane $y = 0$ and its desired shape (circular) upon buckling. Almost all the nodes are in good agreement with the perfect semicircle.

The actuation process is shown in Fig. 11, where the state of gridshell at four time instants (a) $t = 0$ s, (b) $t = 1$ s, (c) $t = 2$ s and (d) $t = 10$ s are displayed. In Fig. 11a, the gridshell is in the state of a 2D network of elastic rods. Then the rod's ends begin to move towards the final circular boundary. At $t = 10$ s in Fig. 11d, the deformation process is complete and the original footprint has buckled into a 3D hemispherical structure. It should be noted that a gravity-like force is applied at the beginning (first 3 seconds) to avoid higher order buckling modes. This jittering force essentially works as an imperfection.

Fig. 14 Design of semi-ellipsoid gridshell based on GA. **a** Variation of fitness value with respect of generation index. **b** Original footprint and final constraint points. **c** Deformed 3D structure and theoretical semi-ellipsoid. **d** Comparison of buckled elastic rod in the plane $y = 0$ and the target semi-ellipsoid. **e** Comparison of buckled elastic rod in the plane $x = 0$ and the target semi-ellipse

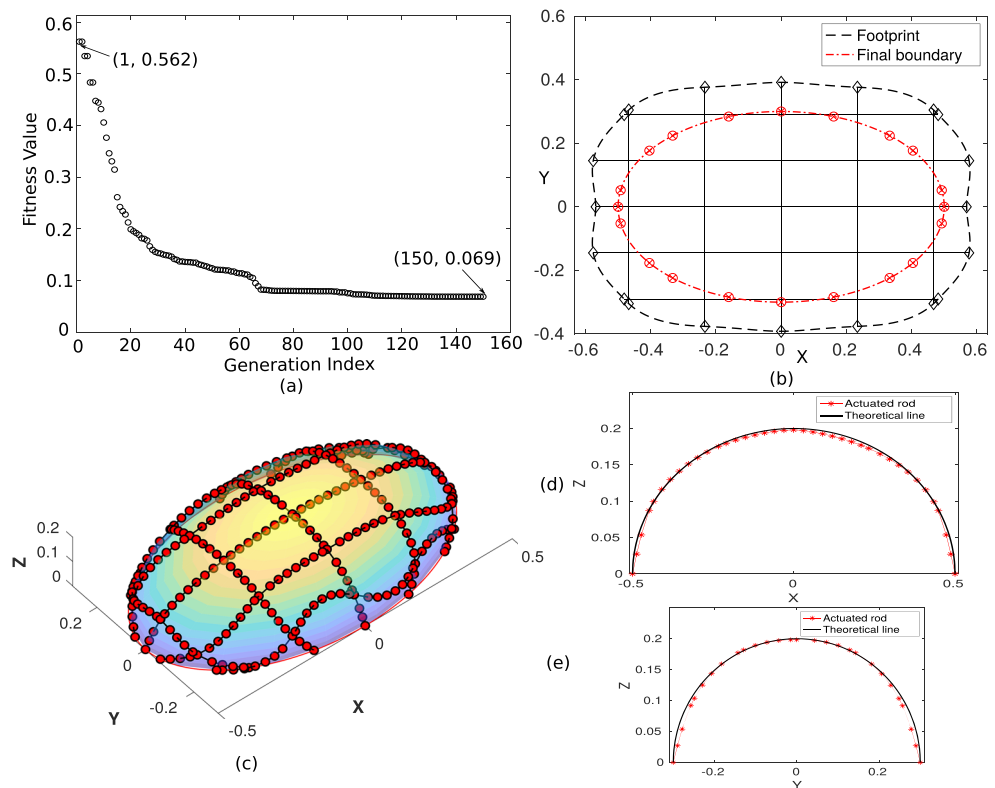


Figure 12 presents the form-finding process in case II, paraboloid. As shown in Fig. 12a, the fast and rough searching process requires only 11 generations and after the 20th generation, the whole population evolves very slowly. The search stops when the fitness value decreases to 0.110 after the 117th generation. Figure 12b shows the original footprint and the final constraint boundary, where the distance between two adjacent and parallel elastic rods is 0.1944 m. According to the comparison in Fig. 12c and d between the deformed 3D structure and the target surface, the footprint and the final constraint boundary found in Fig. 12b are satisfactory.

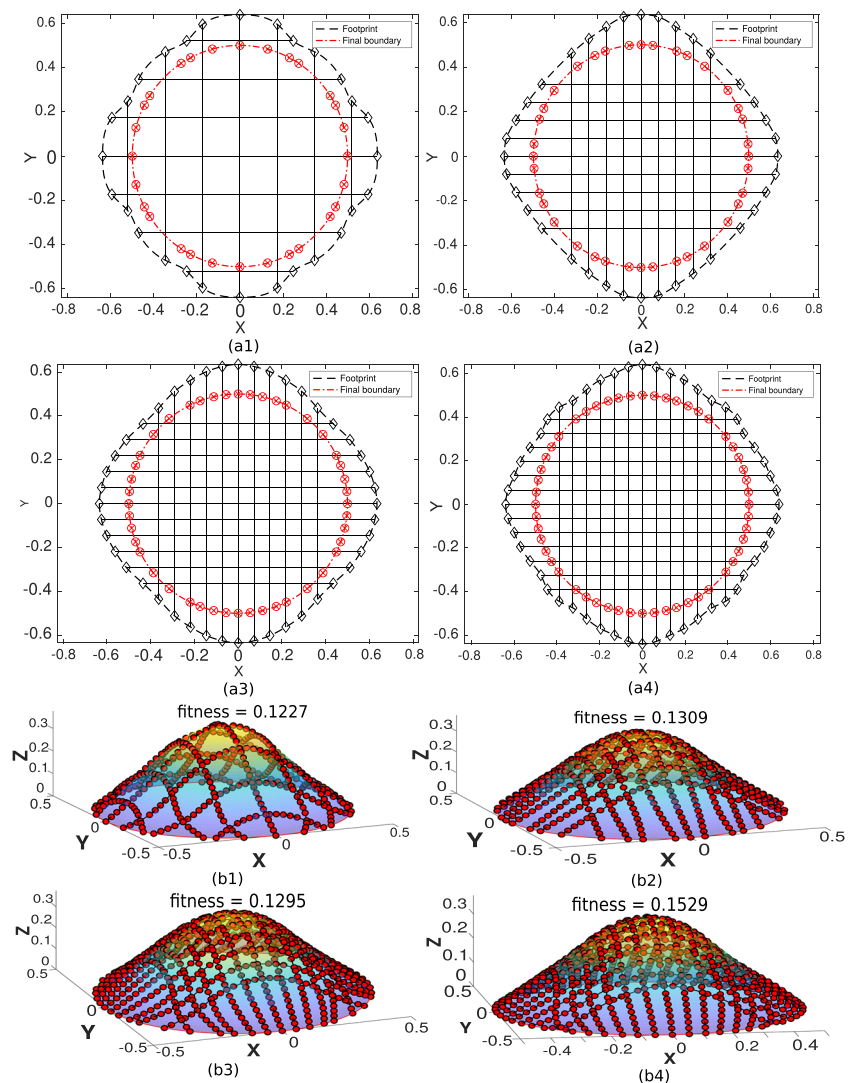
Figure 13 shows the results of the bell-shaped structure, Gaussian surface. In Fig. 13a, the smallest fitness value obtained is 0.128. The footprint and the final constraint boundary are shown in Fig. 13b. Although the final fitness

value is higher than the ones achieved in case I and II, the agreement between the 3D buckled structure and the theoretical Gaussian surface is still satisfactory as shown in Fig. 13c. Comparison between the simulated rod at $y = 0$ and the target line in Fig. 13d also shows that the gridshell is able to rebuild a Gaussian surface when appropriate footprint and final boundary constraint are given.

5.3 Asymmetric case (case IV)

Different from the cases discussed in Section 5.2, semi-ellipsoid is asymmetric about $x = y$ and $x = -y$. Therefore, the number of geometric parameters to be determined has to be increased to 12. For this more complex case, the evolution process correspondingly becomes slow as shown in Fig. 14a. The initial fitness value is 0.562

Fig. 15 Original footprints and final constraint boundary of Gaussian gridshell consisting of 14 elastic rods in (a1), 18 elastic rods in (a2), 22 elastic rods in (a3), and 26 elastic rods in (a4). (b1)~(b4) give their corresponding 3D buckled structure and theoretical surfaces



using the guessed solution from (20a). The whole evolution process stopped after the 150th generation, reaching the maximum threshold of generation number. The final fitness is 0.069. Figure 14b shows the original footprint and the final constraint boundary. Distance between every two adjacent elastic rods is 0.1451 and 0.2337 for rods parallel to the x - and the y -axis, respectively. Unlike the symmetric cases, grids separated by the elastic rods are rectangles instead of squares. Referring to the simulated 3D structure in Fig. 14c, the 3D semi-ellipsoid matches well with the target surface. In Fig. 14 d and e, two buckled elastic rods respectively parallel to the x - and y -axes are displayed to compare with the target curve over the semi-major and the semi-minor axes. It is interesting to note that, as illustrated in Fig. 14b, the original form is not a convex polygon.

5.4 Gridshells consisting of more elastic rods

In the cases above, all the inverse design problems are addressed on the basis of gridshells consisting of 10 elastic rods ($5x + 5y$, i.e., 5 rods along the x -axis and 5 along the y -axis). However, the proposed GA-based inverse design method is not restricted to the number of elastic rods. To design a gridshell consisting of more elastic rods, only a chromosome of larger length is needed to include more geometric parameters. Two genes (and four genes) need to be added when four more elastic rods are added in the symmetric (and asymmetric) cases.

In Fig. 15a1~a4, the footprint and final constraint points of Gaussian surface are evaluated with the GA-based inverse design method for gridshell consisting of 14 ($7x + 7y$), 18 ($9x + 9y$), 22 ($11x + 11y$), and 26 ($13x + 13y$) elastic rods. Their length of chromosome is 8, 10, 12, and 14, respectively. Compared with the footprint in Fig. 13b, the outermost form noticeably changes as more and more elastic rods are added. They are similar to a diamond-like shape and resembles the footprint of a hemisphere. Grid size decreases

from 0.1734 to 0.0650 m as the number of elastic rods increases from 14 to 26.

The 3D buckled structures are shown in Fig. 15b1~b4 when the rods end of footprints are fixed at the constraint points given in Fig. 15a1~a4. All the final fitness values with 10, 14, 18, and 22 elastic rods are around 0.12, but it increases to 0.15 for the 26-rods gridshell. The difference between the simulated shape and the analytical surface is very small and our solution can almost exactly achieve the target shape.

6 Conclusion

In this paper, an improved discrete gridshell model was developed, based on which we proposed a GA-based inverse design method of elastic gridshells. Seven geometric constraints are defined to reduce the input dimension and play a critical role in producing satisfying results. By creating an interface between GA and the discrete gridshell model, online simulation is realized to calculate the fitness value in real-time. Initialized by a feasible guess of individuals, the whole population evolves gradually within 150 generations guided by the fitness function. All these methods and procedures work together to help not only find out the optimal solution but also expedite the optimization process. Three symmetric cases including hemisphere, paraboloid, and Gaussian surface are taken as target structures while another case, semi-ellipsoid, is used as an asymmetric target. With the proposed GA based inverse design method, original footprints and final constraint points are explored to rebuild these shell-like structures. Excellent agreement is achieved between the simulated 3D buckled structure and theoretical surfaces in the above four cases. In the end, the inverse design problem for elastic gridshell consisting of a larger number of rods is explored. The proposed method achieved satisfactory

Table 2 Optimal chromosomes of cases I IV found by the GA-based inverse design method

Target surface	R_{x1}	R_{x2}	θ_{x2}	θ_{x3}	θ_{Fx2}	θ_{Fx3}
Hemisphere	0.782100	0.741047	0.312622	0.695296	0.514617	0.658162
Paraboloid	0.573400	0.552713	0.359345	0.730644	0.433962	0.661161
Gaussian	0.637002	0.639332	0.273912	0.677430	0.105175	0.735382
Semi-ellipsoid	R_{x1}	R_{x2}	θ_{x2}	θ_{x3}	θ_{Fx2}	θ_{Fx3}
	0.568762	0.594331	0.246594	0.542388	0.105817	0.412450
	R_{y1}	R_{y2}	θ_{y2}	θ_{y3}	θ_{Fy2}	θ_{Fy3}
	0.391665	0.442937	1.014903	0.577575	1.055465	0.592478

results even with an increased number of rods and, therefore, a greater number of variables. While the examples in this work were restricted to convex target shapes, future research direction can include more complex shapes and non-planar constraint boundary.

Funding information This work received financial support from the National Science Foundation (Award No. IIS-1925360) and the Henry Samueli School of Engineering and Applied Science, University of California, Los Angeles.

Compliance with ethical standards

Conflict of interest The authors declare that they have no conflict of interest.

Replication of results Details of the GA-based inverse design method of elastic gridshells have been described in Section 4, including the geometric constraints, configuration of GA, population initialization, and the definition of fitness function. The corresponding flowcharts can be found in Figs. 6 and 8. Parameters of the designed surfaces in this paper are available in Section 2. As for the forward deformation process, the DER code could be provided upon request. In order to provide more convenient validation and replication of our findings, the optimal chromosomes corresponding to cases I to IV found by the proposed method are provided in Table 2 that encode the geometry information about the 2D footprint and final shrunk boundary. With these data, the footprint, final shrunk constraint boundary, and the corresponding 3D buckled structures can be replicated.

References

- Baek C, Sageman-Furnas AO, Jawed MK, Reis PM (2018) Form finding in elastic gridshells. *Proc Natl Acad Sci* 115(1):75–80
- Baker JE (1987) Reducing bias and inefficiency in the selection algorithm. In: *Proceedings of the second international conference on genetic algorithms*, vol 206, pp 14–21
- Bergou M, Wardetzky M, Robinson S, Audoly B, Grinspun E (2008) Discrete elastic rods. *ACM Trans Graph (TOG)* 27(3):63
- Bergou M, Audoly B, Vouga E, Wardetzky M, Grinspun E (2010) Discrete viscous threads. In: *ACM Transactions on graphics (TOG)*, vol 29. ACM, p 116
- Bouhaya L, Baverel O, Caron JF (2014) Optimization of gridshell bar orientation using a simplified genetic approach. *Struct Multidiscip Optim* 50(5):839–848
- Chebyshev PL (1946) On the cutting of garments. *Uspekhi Matematicheskikh Nauk* 1(2):38–42
- Coenders J, Bosia D (2006) Computational tools for design and engineering of complex geometrical structures: from a theoretical and a practical point of view. *Game Set And Match II On Computer Games, Advanced Geometries, and Digital Technologies Episode Publishers*, p 006
- Dini M, Estrada G, Froli M, Baldassini N (2013) Form-finding and buckling optimisation of gridshells using genetic algorithms. In: *Proceedings of IASS Annual Symposia, International Association for Shell and Spatial Structures (IASS)*, vol 2013, pp 1–6
- Firl M, Bletzinger KU (2012) Shape optimization of thin walled structures governed by geometrically nonlinear mechanics. *Comput Methods Appl Mech Eng* 237:107–117
- Grinspun E, Desbrun M, Polthier K, Schröder P, Stern A (2006) Discrete differential geometry: an applied introduction. *ACM SIGGRAPH Course* 7:1–139
- Hajela P, Lee E (1995) Genetic algorithms in truss topological optimization. *Int J Solids Struct* 32(22):3341–3357
- Jawed MK, Da F, Joo J, Grinspun E, Reis PM (2014) Coiling of elastic rods on rigid substrates. *Proc Natl Acad Sci* 111(41):14663–14668
- Jawed MK, Khouri N, Da F, Grinspun E, Reis PM (2015) Propulsion and instability of a flexible helical rod rotating in a viscous fluid. *Phys Rev Lett* 115(16):168101
- Jawed MK, Novelia A, O'Reilly OM (2018) A primer on the kinematics of discrete elastic rods. Springer
- Jiang Y, Zegard T, Baker WF, Paulino GH (2018) Form-finding of grid-shells using the ground structure and potential energy methods: a comparative study and assessment. *Struct Multidiscip Optim* 57(3):1187–1211
- Kirchhoff G (1859) Über das gleichgewicht und die bewegung eines unendlich dunnen elastischen stabes. *J Reine Angew Math* 56:285–313
- Koohestani K (2012) Form-finding of tensegrity structures via genetic algorithm. *Int J Solids Struct* 49(5):739–747
- Lefevre B, Douthé C, Baverel O (2015) Buckling of elastic gridshells. *J Int Assoc Shell Spatial Struct* 56(3):153–171
- Mitchell M (1998) An introduction to genetic algorithms. MIT press
- Pai DK (2002) Strands: interactive simulation of thin solids using cosserat models. In: *Computer graphics forum*, vol 21. Wiley Online Library, pp 347–352
- Panetta J, Konaković-Luković M, Isvoranu F, Bouleau E, Pauly M (2019) X-shells: a new class of deployable beam structures. *ACM Trans Graph (TOG)* 38(4):1–15
- Pérez J, Thomaszewski B, Coros S, Bickel B, Canabal JA, Sumner R, Otaduy MA (2015) Design and fabrication of flexible rod meshes. *ACM Trans Graphics (TOG)* 34(4):1–12
- Quagliaroli M, Malerba P (2013) Flexible bridge decks suspended by cable nets. A constrained form finding approach. *Int J Solids Struct* 50(14–15):2340–2352
- Richardson JN, Adriaenssens S, Coelho RF, Bouillard P (2013) Coupled form-finding and grid optimization approach for single layer grid shells. *Eng Struct* 52:230–239
- Rojas R (2013) Neural networks: a systematic introduction. Springer Science & Business Media
- Shimoda M, Yamane K (2015) A numerical form-finding method for the minimal surface of membrane structures. *Struct Multidiscip Optim* 51(2):333–345
- Shimoda M, Yamane K, Shi JX (2018) Non-parametric shape optimization method for designing cable net structures in form finding and stiffness maximization problems. *International Journal of Solids and Structures*
- Spillmann J, Teschner M (2009) Cosserat nets. *IEEE Trans Visual Comput Graph* 15(2):325–338
- Su Y, Ohsaki M, Wu Y, Zhang J (2019) A numerical method for form finding and shape optimization of reciprocal structures. *Eng Struct* 198:109510
- Tayeb F, Caron JF, Baverel O, Du Peloux L (2013) Stability and robustness of a 300 m2 composite gridshell structure. *Construct Build Mater* 49:926–938
- Veenendaal D, Block P (2012) An overview and comparison of structural form finding methods for general networks. *Int J Solids Struct* 49(26):3741–3753
- Winslow P, Pellegrino S, Sharma S (2010) Multi-objective optimization of free-form grid structures. *Struct Multidiscip Optim* 40(1–6):257
- Xu S, Yan Z, Jang KI, Huang W, Fu H, Kim J, Wei Z, Flavin M, McCracken J, Wang R et al (2015) Assembly

of micro/nanomaterials into complex, three-dimensional architectures by compressive buckling. *Science* 347(6218):154–159

Xu Z, Fan Z, Fu H, Liu Y, Zi Y, Huang Y, Zhang Y (2019) Optimization-based approach for the inverse design of

ribbon-shaped three-dimensional structures assembled through compressive buckling. *Phys Rev Appl* 11(5):054053

Publisher's note Springer Nature remains neutral with regard to jurisdictional claims in published maps and institutional affiliations.